This is the author's version of an article that has been published in the IEEE RoboSoft proceedings.
Changes were made to this version by the publisher prior to publication.
The final version of record is available at https://doi.org/10.1109/RoboSoft55895.2023.10122047

Towards a Modular Framework for Visco-Hyperelastic Simulations of Soft Material Manipulators with Well-Parameterised Material

Max Bartholdt*, Rebecca Berthold and Moritz Schappler

***Abstract*— Controller design for continuum robots maintains to be a difficult task. Testing controllers requires dedicated work in manufacturing and investment into hardware as well as software, to acquire a test bench capable of performing dynamic control tasks. Typically, proprietary software for practical controller design such as MATLAB/SIMULINK is used but lacks specific implementations of soft material robots.**
This intermediate work presents the results of a toolchain to derive well-identified rod simulations. State-of-the-art methods to simulate the dynamics of continuum robots are integrated into an object-oriented implementation and wrapped into the SIMULINK framework. The generated S-function is capable of handling arbitrary, user-defined input such as pressure actuation or external tip forces as demonstrated in numerical examples. With application to a soft pneumatic actuator, stiffness parameters of a nonlinear hyperelastic material law are identified via finite element simulation and paired with heuristically identified damping parameters to perform dynamic simulation. To prove the general functionality of the simulation, a numerical example as well as a benchmark from literature is implemented and shown. A soft pneumatic actuator is used to generate validation data, which is in good accordance with the respective simulation output. The tool is provided as an open-source project.**

I. INTRODUCTION

The field of continuum robotics has been inspired by the inherent compliance of the systems, suited for safe human-robot interaction. Especially manipulators manufactured from soft materials such as silicone-based polymers have gained rising popularity in the robotics community. In the recent years, several toolboxes for modelling of soft continuum manipulators were published, based on various approaches [1]. They differ in their goals such as fast simulations for re-enforcement learning approaches [2], working towards coherent multi-flexible-body system frameworks and control application [3], [4], [5], [6], full-body deformation analyses, control, and topology optimisation [7] and system analysis with coupled structures [8]. At the centre of each simulation lies the trade-off between the accuracy and computational efficiency of numerical methods solving a set of partial or ordinary differential equations (PDE/ODE). Therefore, model order reduction techniques are applied to decrease the system's total degrees of freedom (DoF), one of them being the dimensional reduction from 3D body configurations to 1D beam representations of slender objects, i.e. soft robotic manipulators.

By experimental validation, the Cosserat rod theory, as one representative of possible dimensional reductions, has repeatedly been proven to be a valid choice for describing slender structures for continuum robots [9], [10], including pneumatically driven silicone-based actuator modules [11], [12]. The shooting method has been a popular choice and has shown capabilities of fast simulations [10]. The implementations provided by Till et al. are a stepping stone toward more detailed models in simulation.

A. Preliminary work

Based on Till's works, investigation of phenomena occurring during pressurisation of soft pneumatic actuators

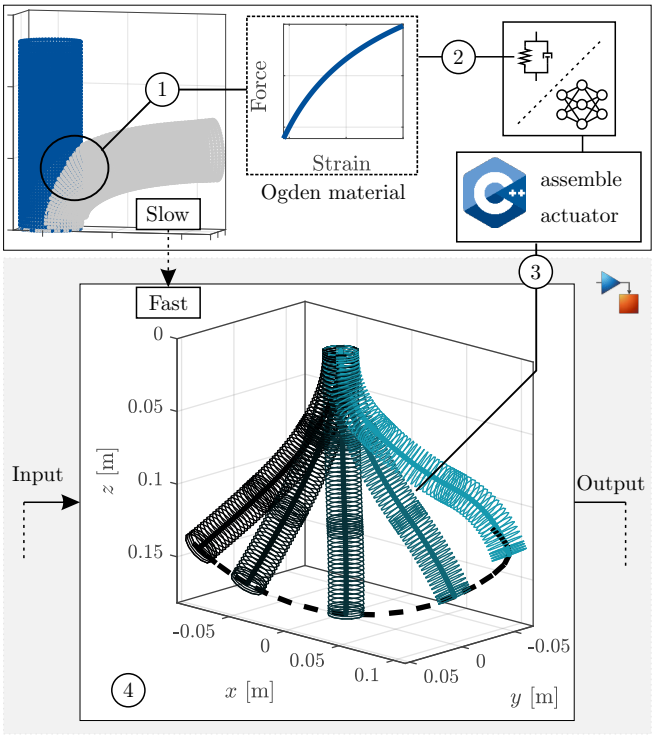

Fig. 1. The toolchain is schematically portrayed. (1) From FE simulation parameters for nonlinear hyperelastic materials are found. (2) Those are used to implement a Kelvin-Voigt model of which the inverse map is learned. (3) Inverse material functions are exported into an object-oriented C++ implementation where the SPAs are assembled. (4) Multiple SPAs are simulated within Simulink using a fixed-step discrete-time solver.

* Corresponding author. All authors are with the Leibniz University of Hannover, Institute of Mechatronic Systems, 30823 Garbsen, Germany. Contact: max.bartholdt@imes.uni-hannover.de

Funded by the Deutsche Forschungsgemeinschaft (DFG, German Research Foundation) under grant no. 405032969.

** Code available under https://gitlab.com/soft_material_robotics/cosserat-rod-simulink-sfunction

TABLE I
MODELS USING NONLINEAR ELASTICITY AND/OR A COMBINATION OF NONLINEAR ELASTICITY AND VISCOSITY

Ref.	Kinematic	NL-HE	NL Visco-HE
[18]	PCC	✓	✓
[19]	CC	✓	✓
[20]	PCC	✓	–
[2]	Kinematic chains	–	–
[8]	Discrete elastic rods	–	–

have been conducted within the authors' research project [13], [14], [15]. Different approaches for handling nonlinear effects of material and pressure actuation in static Cosserat rod models, solved using the shooting method, are presented.

The works of [16] in contrast implement an Ogden material model (OM) for a variational Simo-Reissner beam formulation and identify parameters as well as a mapping for pressure to actuation forces with help of various experiments, showing good accordance between simulation and results from the test bench. The topic of nonlinear (NL) hyperelasticity (HE) for structural models has gained a substantial rise in attention, mostly due to its application in soft-material robotics [17]. It has also been discussed in various publications for models with varying kinematic assumptions, which are listed in Table I (excluding finite element (FE) approaches).

Specifically in low-dimensional approaches using (piecewise) constant curvature (PCC/CC), nonlinear elasticity is often used, to approximate the general behaviour of the potential energy. For the more complex kinematics of structural models, nonlinear hyperelasticity has also been examined [20]. However, based on various experiments conducted using a soft pneumatic actuator (SPA), the best results were achieved using a Hookean (linear) constitutive equation to computed strains. Still, separating nonlinear effects of the material, or other ones as observed in [15] is important for accurate modelling. With the previous works, it is shown that, given the correct material description, identification of parameters and mapping of actuation forces as well as accurate and efficient simulation of soft-material manipulators is possible.

The problems in the context of the shooting method are how to *implement nonlinear (visco-)hyperelastic materials* in a computationally efficient matter and how to parametrise them. Furthermore, the implementations should target a generalising structure, capable of simulating different geometries and multiple actuators with varying material properties.

B. Contribution and Structure of this Paper

Presented in this paper is an intermediate result of a coherent methodology, as depicted in Fig. 1, leading to well-parametrised simulations of soft-material robots (SMR) based on the works of [10]. The foundation of the methodology is a library of material data from stress-strain experiments. Integrated into FE simulation, a detailed model of an actuator is set up in ABAQUS [15]. Providing detailed insight into deformation behaviour comes at the cost of a high computational burden, especially when it comes to dynamics. A dimensional reduction, and thereby gain in computational efficiency, is achieved by using Cosserat rod models.

Constitutive equations in rod models contain parameters which if chosen incorrectly lead to a poor approximation of the reality [13] or more detailed simulations. This is tackled, by numerically reducing the data from FE simulation and computing kinematic components describing Cosserat rods. Parameters for respective material laws are then identified using the exported local body forces/moments and local displacements. This is demonstrated for a nonlinear OM presented in [16]. Finding these accurate rod material parameters, that generalize the behaviour of the actuator in different loading conditions in experiments is a cumbersome task, which as we show in this paper can then be omitted.

With this work, a simulation framework is introduced. The framework is integrated into MATLAB/SIMULINK to quickly set up dynamics simulations and evaluate their results. Including the OM in the popular shooting method leads to a substantial rise in computation time due to nonlinear solving for deformation parameters at each integration step. This is solved by applying an approximation of the inverse material equations using simple four-layer feed-forward neural networks. Summarising this paper's contributions, we are

- providing a coherent methodology to identify necessary parameters of the proposed Ogden model in [16] without extensive experiments,
- extending the nonlinear hyperelasticity by integrating it in a Kelvin-Voigt material model,
- implementing the material models into the numerical scheme of [10] without loss of computational efficiency,
- and validating the simulation with experiments.

The paper is structured as follows. The second section includes theoretical and numerical modelling aspects of Cosserat rods with (visco-)hyperelastic material as well as a brief review on works investigating nonlinear hyperelasticities. Thereafter in Sec. III, the data export and computation required for the proposed identification strategy of the hyperelasticity is performed using point-cloud registration. In Sec. IV, we show experiments in which dynamics parameters are still tuned heuristically, but show good accordance with the simulation. In Sec. V numerical examples are demonstrated on the one-hand side for verifying benchmarks from the literature and on the other side for showing the capabilities of the tool.

The simulation was implemented object-oriented, based on provided code in C++ and moulded into a CMake project, which is capable of automatically generating S-Functions for MATLAB/SIMULINK integration. All code of this publication is made publicly available and is subject to the authors' future work.

II. MODELLING

A. Cosserat Rod

This section briefly reviews the governing equations of motion for a Cosserat rod. The theory is equivalent to the

Simo-Reissner theory of beams undergoing large deflections [16]. The configuration of the deformed slender structure at time t is described, as the spatial curve $\boldsymbol{r}(s,t)$ and the orientation of cross-sections expressed by $\boldsymbol{R}(s,t) \in SO(3)$. Derivatives in spatial and time domain s and t are given by

$$\boldsymbol{r}_s = \boldsymbol{R}\boldsymbol{v}, \qquad \boldsymbol{r}_t = \boldsymbol{R}\boldsymbol{q}, \tag{1}$$

$$\boldsymbol{R}_s = \boldsymbol{R}\boldsymbol{S}(\boldsymbol{u}), \qquad \boldsymbol{R}_t = \boldsymbol{R}\boldsymbol{S}(\boldsymbol{\omega}), \tag{2}$$

with local strains $\boldsymbol{v}(s,t)$ and $\boldsymbol{u}(s,t)$ and local velocity $\boldsymbol{q}(s,t)$ and angular velocity $\boldsymbol{\omega}(s,t)$. The skew-symmetric cross-product operator is denoted by $\boldsymbol{S}() \in so(3)$. The rate of change of the local velocity and angular velocity w.r.t. the material coordinate s is

$$\boldsymbol{q}_s = \boldsymbol{v}_t - \boldsymbol{S}(\boldsymbol{u})\boldsymbol{q} + \boldsymbol{S}(\boldsymbol{\omega})\boldsymbol{v} \tag{3}$$

$$\boldsymbol{\omega}_s = \boldsymbol{u}_t - \boldsymbol{S}(\boldsymbol{u})\boldsymbol{\omega} \quad . \tag{4}$$

The force and moment balance equations on an infinitesimal section of the rod lead to the differential expression for the change of forces and moments

$$\boldsymbol{n}_s = \rho A \boldsymbol{R}\left(\boldsymbol{S}(\boldsymbol{\omega})\boldsymbol{q} + \boldsymbol{q}_t\right) - \boldsymbol{f} \tag{5}$$

$$\boldsymbol{m}_s = \rho \boldsymbol{R}\left(\boldsymbol{J}\boldsymbol{\omega}_t + \boldsymbol{S}(\boldsymbol{\omega})\boldsymbol{J}\boldsymbol{\omega}\right) + \boldsymbol{S}(\boldsymbol{n})\boldsymbol{r}_s - \boldsymbol{l} \tag{6}$$

with external distributed loads $\boldsymbol{f}(s,t)$, moments $\boldsymbol{l}(s,t)$, inner forces $\boldsymbol{n}(s,t)$ and moments $\boldsymbol{m}(s,t)$. Further, ρ is the material density, A is the area of the cross-section and $\boldsymbol{J}$ is the rotational inertia associated with each cross-section.

The linear elastic material behaviour is described by the constitutive equations

$$\boldsymbol{n} = \boldsymbol{R}\left[\boldsymbol{K}_{\mathrm{se}}\left(\boldsymbol{v} - \boldsymbol{v}^*\right) + \boldsymbol{B}_{\mathrm{se}}\boldsymbol{v}_t\right] \tag{7}$$

$$\boldsymbol{m} = \boldsymbol{R}\left[\boldsymbol{K}_{\mathrm{bt}}\left(\boldsymbol{u} - \boldsymbol{u}^*\right) + \boldsymbol{B}_{\mathrm{bt}}\boldsymbol{u}_t\right] \quad , \tag{8}$$

where $\boldsymbol{K}_{\mathrm{se}}$ and $\boldsymbol{K}_{\mathrm{bt}}$ are diagonal matrices describing the stiffness for shear, extension, bending and torsion respectively. The corresponding diagonal damping matrices are $\boldsymbol{B}_{\mathrm{se}} = \mathrm{diag}\left(b_{\mathrm{s}}, b_{\mathrm{s}}, b_{\mathrm{e}}\right)$ and $\boldsymbol{B}_{\mathrm{bt}} = \mathrm{diag}\left(b_{\mathrm{b}}, b_{\mathrm{b}}, b_{\mathrm{t}}\right)$. In this work only initially straight rods are considered leading to $\boldsymbol{v}^*(s) = [0,\, 0,\, 1]^{\mathrm{T}}$ and pre-curvature $\boldsymbol{u}(s) = [0,\, 0,\, 0]^{\mathrm{T}}$.

B. Shooting Method

To solve the given PDE (2)–(6) quickly, the proposed method in [10] is applied. First, the implicit discretisation of the time domain leads to a semi-discretised set of ODEs. The time derivatives are then given by

$$\boldsymbol{v}_t = c_0\boldsymbol{v} + \overset{\mathrm{h}}{\boldsymbol{v}}, \qquad \boldsymbol{u}_t = c_0\boldsymbol{u} + \overset{\mathrm{h}}{\boldsymbol{u}}, \tag{9}$$

$$\boldsymbol{q}_t = c_0\boldsymbol{q} + \overset{\mathrm{h}}{\boldsymbol{q}}, \qquad \boldsymbol{\omega}_t = c_0\boldsymbol{\omega} + \overset{\mathrm{h}}{\boldsymbol{\omega}}, \tag{10}$$

where quantities from previous time steps are summed up and denoted with $\overset{\mathrm{h}}{*}$ and c_0 is dependent on the choice of BDF-α method and time step Δt.

The boundary-value problem of the spatial domain at each time step is then reformulated to an optimization problem of a set of initial values. Numerical integration is performed on a unit quaternion representation of the orientation and by using a second-order Runge-Kutta method. For the residual of a serially-connected structure of rods with a clamped base and a loose end follows

$$\boldsymbol{x}^{\mathrm{T}}(\boldsymbol{n}_0, \boldsymbol{m}_0) = \begin{pmatrix} (\boldsymbol{n}^* - \boldsymbol{n}_N)^{\mathrm{T}} & (\boldsymbol{m}^* - \boldsymbol{m}_N)^{\mathrm{T}} \end{pmatrix} \tag{11}$$

with $\boldsymbol{n}^*$ and $\boldsymbol{m}^*$ being external forces at the last node N of the discrete rod.

C. Constitutive Equations

In this paper, the energy-density function of [16] and its identified parameters are reused and extended by a linear viscosity resulting in a visco-hyperelastic relationship for extensional and bending deformations. The partial derivatives of the hyperelastic strain-density function

$$W = \frac{2\,\mathrm{EA}\,c_{\mathrm{e}}}{3\,\alpha^2}\left(\lambda(\boldsymbol{v})^{\alpha} + \frac{2}{\lambda(\boldsymbol{v})^{\alpha/2}} - 3\right) \tag{12}$$

w.r.t. the kinematic strain variables $\boldsymbol{v} = [v_1,\, v_2,\, v_3]^{\mathrm{T}}$ are the constitutive equations to calculate inner forces

$$\boldsymbol{R}^{\mathrm{T}}\boldsymbol{n} = \begin{pmatrix} k_s\, v_1 + \dfrac{2\,\mathrm{EA}\,c_{\mathrm{e}}\, v_1\left(\left({v_1}^2+{v_2}^2+{v_3}^2\right)^{\frac{3\alpha}{4}} - 1\right)}{3\,\alpha\left({v_1}^2+{v_2}^2+{v_3}^2\right)^{\frac{\alpha}{4}+1}} \\ k_s\, v_2 + \dfrac{2\,\mathrm{EA}\,c_{\mathrm{e}}\, v_2\left(\left({v_1}^2+{v_2}^2+{v_3}^2\right)^{\frac{3\alpha}{4}} - 1\right)}{3\,\alpha\left({v_1}^2+{v_2}^2+{v_3}^2\right)^{\frac{\alpha}{4}+1}} \\ \dfrac{2\,\mathrm{EA}\,c_{\mathrm{e}}\, v_3\left(\left({v_1}^2+{v_2}^2+{v_3}^2\right)^{\frac{3\alpha}{4}} - 1\right)}{3\,\alpha\left({v_1}^2+{v_2}^2+{v_3}^2\right)^{\frac{\alpha}{4}+1}} \end{pmatrix} \tag{13}$$

in local reference frame. Parameters k_s and EA are the shear and extensional stiffness calculated with literature and geometric parameters, while stiffness scaling c_{e} and α are to be identified. Bending and torsional deformations are described with a Kelvin-Voigt material behaviour and thereby linear elastic. Extending (13) to dynamics yields

$$\boldsymbol{R}^{\mathrm{T}}\boldsymbol{n} = \boldsymbol{N}_{\mathrm{hyp}}(\boldsymbol{v}) + \boldsymbol{B}_{\mathrm{se}}\boldsymbol{v}_t \tag{14}$$

with the nonlinear expression $\boldsymbol{N}_{\mathrm{hyp}}$ describing the right-hand side of (13). Applying the proposed implicit time discretisation in [10] results in

$$\boldsymbol{R}^{\mathrm{T}}\boldsymbol{n} = \boldsymbol{N}_{\mathrm{hyp}}(\boldsymbol{v}) + \boldsymbol{B}_{\mathrm{se}}(c_0\boldsymbol{v} + \overset{\mathrm{h}}{\boldsymbol{v}}) \quad . \tag{15}$$

Following the numerical scheme of [10], the history terms $\overset{\mathrm{h}}{\boldsymbol{v}}\,(s_i)$ and local forces $\boldsymbol{R}^{\mathrm{T}}\boldsymbol{n}$ are known quantities, when it comes to solving this equation for deformation quantities $\boldsymbol{v}(\boldsymbol{s})$ at any discrete node s_i. The next section introduces a simple method to solve this nonlinear equation computationally efficiently to maintain the simulation's high real-time ratio using the shooting method.

D. Inverse Constitutive Equations

The inverse function of (13) has to be solved at every integration step of the spatial domain. Due to the high computational burden of using an iterative solver like the multi-dimensional Newton-Raphson method, instead, the function is evaluated for a relevant data subset $V_{\mathrm{d}} \subset \mathbb{R}^3$ and a simple four-layer feedforward neural network (NN) is used to approximate the relationship between the respective function values $\boldsymbol{n}_{\mathrm{d}}$ and function arguments $\boldsymbol{v}_{\mathrm{d}} \in V_{\mathrm{d}}$. Note that as

This is the author's version of an article that has been published in the IEEE RoboSoft proceedings.
Changes were made to this version by the publisher prior to publication.
The final version of record is available at https://doi.org/10.1109/RoboSoft55895.2023.10122047

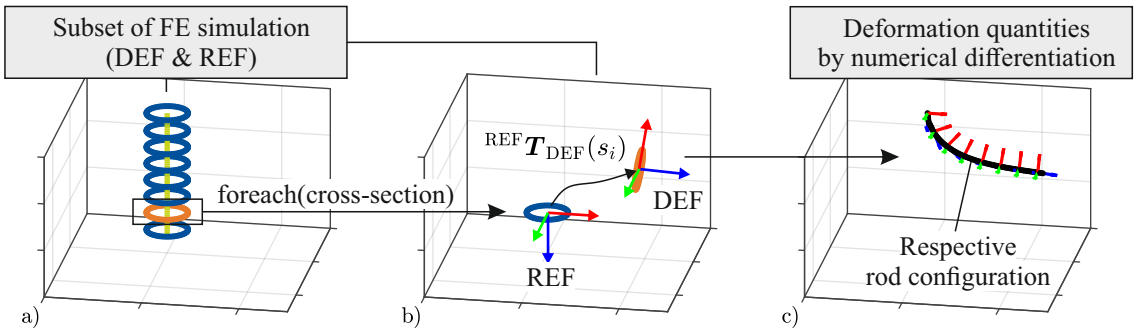

Fig. 2. Data conversion for Identification. a) The circular subsets X_{CS} are shown. The subsets are parsed to b), where an iterative registration between the point clouds in REF and DEF is performed. Finally, in c) the slender representation is reconstructed and deformation quantities are gained by numerical differentiation.

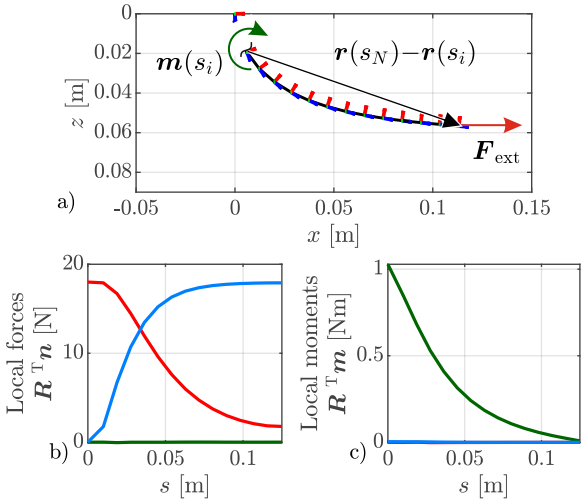

Fig. 3. a) Computed deformations and computation of local moments. b,c) local forces $\boldsymbol{R}^{\mathrm{T}}\boldsymbol{n}$ and moments $\boldsymbol{R}^{\mathrm{T}}\boldsymbol{m}$ over material coordinate s for a load case of 10 N in x-direction.

long as all rod deformation states $\boldsymbol{v}$ in the simulation are within the closed boundaries of V_{d}, the capability of the NN to extrapolate is not of concern. The only purpose of the NN here is to give fast solutions of a known domain so that it is sufficient to show its performance in interpolating the provided data.

III. PARAMETER IDENTIFICATION

Performing experiments to find valid parameters for rod models, as it was done in [16], is time-consuming and not efficient regarding the design and development of soft-material manipulators. Therefore, the goal of the presented methods in this section is to find parameters for beam material models from accurate, validated FE simulation in an efficient matter.

A. Finite Element Method

The finite element method (FEM) used to identify the material parameters is set up in the software ABAQUS. This FEM models the SPA on a detailed level and includes three silicone parts and six fibres used to reinforce each chamber.

TABLE II
NUMERIC VALUES OF PARAMETERS FOUND IN IDENTIFICATION OR HEURISTICALLY (DAMPING)

EA	α	c_{e}	$c_{\mathrm{s}}GA$
91.87 N	1.3308	2.2703	88.566 N
b_{e}	b_{s}	b_{b}	b_{t}
10 N s	10 N s	0.0855 mN m s	0.04 N m s
EI_{xx}	EI_{yy}	GI_{T}	
0.0257 N m^2	0.0257 N m^2	0.0291 N m^2	

For the silicone body part as well as the caps the hyperelastic OM is used. The main body part consists of the soft silicone Ecoflex 0050 while the caps are made of Dragonskin 30 [15], which is noticeably stiffer. For the simulation, the SPA is clamped at its base. A reference point is placed on the tip surface and coupled to the nodes on the inner circumference of the tip. Hence the deformation of these nodes is prevented. For parameter identification, two separated external forces acting in z- and x-direction are applied to the reference point. The forces are incrementally raised to 98 N in z-direction and 18 N in x-direction (cf. Fig. 3 for definition). No pressure or gravitational loads were applied in the simulations. The FE simulation output for the SPA was validated against data from experiments showing slightly softer behaviour when elongating in the axial direction and slightly stiffer behaviour in bending experiments with pressure actuation [21].

B. Data Conversion

Finding parameters α and c_{e} in (12) requires data on local strains $\boldsymbol{v}(s)$, $\boldsymbol{u}(s)$, local forces $\boldsymbol{R}^{\mathrm{T}}\boldsymbol{n}(s)$ and local moments $\boldsymbol{R}^{\mathrm{T}}\boldsymbol{m}(s)$. Given by the FE simulations is the reference configuration (REF) $\boldsymbol{X} \in \mathbb{R}^{N\times 3}$ and deformed configuration (DEF) $\boldsymbol{\varphi}(\boldsymbol{X}) \in \mathbb{R}^{N\times 3}$ with N spatial points respectively. Therefore, a numerical reduction to a spatial curve $\boldsymbol{r}_0(s)$ with cross-sections represented by $\boldsymbol{R}_0(s)$ in REF and the analogue quantities in DEF are required.

To perform the numerical dimensional reduction, depicted in Fig. 2, with the goal to compute local strains $\boldsymbol{v}(s)$ and

This is the author's version of an article that has been published in the IEEE RoboSoft proceedings.
Changes were made to this version by the publisher prior to publication.
The final version of record is available at https://doi.org/10.1109/RoboSoft55895.2023.10122047

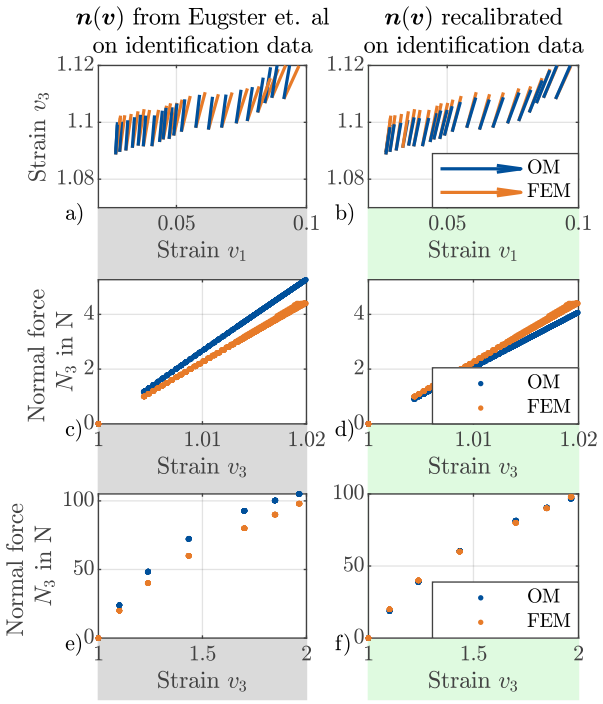

Fig. 4. Comparison of results of identification for Ogden material (left column Eugster et al., right column identification with FE data). a) and b) showing vector fields $\boldsymbol{n}(\boldsymbol{v})$ for max. load of F_{ext} 10 N and 0.05 m$<s<$0.10 m. c) and d) show a comparison of both sets of parameters on low deformation and e) and f) on high deformation for 0.03 m$<s<$0.10 m.

$\boldsymbol{u}(s)$, the mantle of the cylindrical actuator (radius R), i.e. a subset

$$\boldsymbol{X}_{\text{R}} = \{\boldsymbol{x}_i \in \boldsymbol{X} \,|\, x_{i1}^2 + x_{i2}^2 = R^2\} \quad i \in 1, ..., N \quad . \tag{16}$$

in REF, is used to find further subsets of N cross-sections, given by

$$\boldsymbol{X}_{\text{CS},i} = \{\boldsymbol{x}_{\text{R},i} \in \boldsymbol{X}_{\text{R}} \,|\, x_{\text{R},i3} = s_i\} \quad i \in 1, ..., N \quad . \tag{17}$$

At this point, it is assumed that cross-sections are rigid. The homogeneous rigid transformations $\boldsymbol{T}(s_i) \in SE(3)$ with

$$\boldsymbol{X}_{\text{CS},i} = {}^{\text{REF}}\boldsymbol{T}_{\text{DEF}}(s_i)\boldsymbol{\varphi}(\boldsymbol{X}_{\text{CS},i}) \tag{18}$$

are found via rigid point-cloud registration [22] (Fig. 2b).

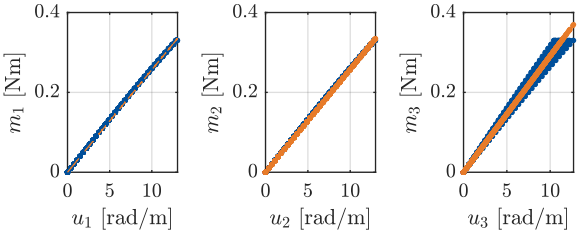

Fig. 5. Results (orange) of identification of bending stiffness using FE simulation data (blue).

Local change in orientation $\boldsymbol{u}$ is then computed as

$$\boldsymbol{S}(\boldsymbol{u}_i) = \frac{1}{s_i}\text{logm}\left(\boldsymbol{R}^{\text{T}}(s_i)\boldsymbol{R}(s_{i+1})\right) \tag{19}$$

with $\boldsymbol{R}(\cdot) \in SO(3)$ being the rotational part of $\boldsymbol{T}(s_i)$ and $\text{logm}\,(*)$ denoting the matrix logarithm. The centre line $\boldsymbol{r}$ in DEF is computed by

$$\boldsymbol{r}_i = \boldsymbol{R}(s_i)\boldsymbol{r}_0(s_i) + \boldsymbol{t}_i \tag{20}$$

with the translation $\boldsymbol{t}_i$ found from point-cloud registration. Local deformations $\boldsymbol{v}_i$ are computed via finite differences by

$$\boldsymbol{v}_i = \boldsymbol{R}^{\text{T}}(s_i)\frac{\Delta \boldsymbol{r}_i}{\Delta s_i} \quad . \tag{21}$$

For simple load cases such as external tip forces/moments, the local forces are simply computed by assuming constant force along the structure and projecting it into the respective frame defined by $\boldsymbol{R}(s_i)$. Moments in the global frame are calculated as depicted in Fig. 3 by

$$\boldsymbol{m}(s_i) = \boldsymbol{m}_{\text{ext}} + (\boldsymbol{r}_N - \boldsymbol{r}_i) \times \boldsymbol{F}_{\text{ext}} \tag{22}$$

accordingly.

C. Identification Results

By using the LEVENBERG-MARQUARDT optimisation algorithm implemented in MATLAB and the data exported from the FEM, parameters listed in Table II are identified. The parameters found in experiments and originally presented in [16] as well as parameters found by identification from FE simulations are used to produce the results in Fig. 4. In the simulations including vertical loads, shear deformation in the Ecoflex 0050 section of the manipulator reaches up to 9%. Shearing stiffness is scaled by 2.891 leading to stiffer results than Eugster et al. (Fig. 4 a)–b)). For parameters α and c_{e}, both approaches lead to similar values. The deviation from FE models to the real system partially explains the difference and is in accordance with the findings in the validation of

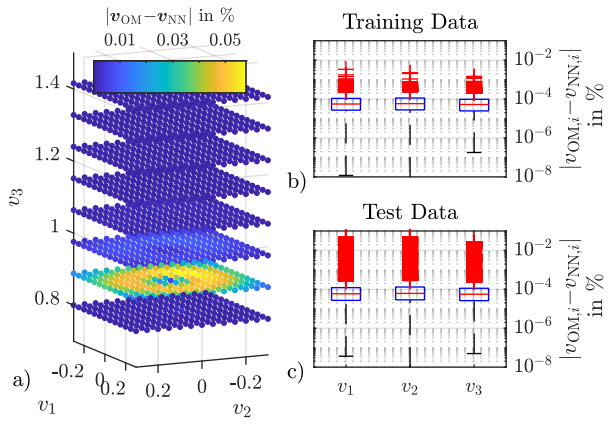

Fig. 6. Results of the regression of the inverse function via FFNN. In a) the color map indicates the prediction error on a test set evenly distributed in between the training data. Both b) and c) show the component-wise absolute error between deformations $\boldsymbol{v}_{\text{OM}}$ and $\boldsymbol{v}_{\text{NN}}$ (see Eq. 23).

This is the author's version of an article that has been published in the IEEE RoboSoft proceedings.
Changes were made to this version by the publisher prior to publication.
The final version of record is available at https://doi.org/10.1109/RoboSoft55895.2023.10122047

the FE model. Fig. 4 c)–d) show the OM and FEM data for small elongations (0–2 %) and e)–f) for elongation up to 100 %. In the absence of large deformations, the stress-strain relationship is visibly linear. For strains within the range of 0 to 100% in Fig. 4 e) and f), a noticeable reduction of the stiffness is observed, which is in accordance with material results presented in [15].

For identification of bending parameters, an external tip moment of up to 350 N mm is applied for each rotational DoF. The bending data used for identification shows a linear relationship (see Fig. 5) with a scaling factor of 2.061.

D. Neural Network Training

With the analytical model and identified parameters, a set of input-output values as described in Sec. II-D is generated. The feed-forward neural network (FFNN) interpolates the data to learn the inverse function since analytical inversion is not possible and numerical solving computationally expensive. MATLAB's *deep-learning toolbox* is used to configure a four-layer network with 20 neurons each. The hyperbolic tangent function is used as the activation function. Training is conducted using a data set $V_{\mathrm{OM,Tr}}$ of 2000 samples $\boldsymbol{v}_{\mathrm{OM},i}$ evenly distributed in the intervals $v_1, v_2 \in [-0.3, 0.3]$ and $v_3 \in [0.8, 3.0]$, including compressional load.

Fig. 6 shows the result on training and test data. The output of the analytical OM for training data $V_{\mathrm{OM,Tr}}$ and test data $V_{\mathrm{OM,Te}}$ is input argument to the FFNN $\boldsymbol{f}_{\mathrm{NN}}$ such that the prediction results to

$$\boldsymbol{v}_{\mathrm{NN}} = \boldsymbol{f}_{\mathrm{NN}}(\boldsymbol{N}_{\mathrm{hyp}}(\boldsymbol{v}_{\mathrm{OM}})) \quad . \tag{23}$$

$V_{\mathrm{OM,Te}}$ is defined for the same intervals as $V_{\mathrm{OM,Tr}}$ but contains 4394 evenly distributed samples. Therefore, the samples lie in between the training data and reflect on how well the FFNN interpolates.

The absolute deviation between inverse OM and FFNN shows a median of less than 10×10^{-4} % on training (Fig. 6 a) and test data (Fig. 6 b). Outliers in test data reach up to approx. 0.05 % deformation. For an integration step in spatial domain with a typical step size around 0.01 m this leads to an approximate positioning error of 0.5 µm. Fig. 6 a) indicates, that most outliers occur systematically for compression ($v_3 < 1$). Further investigations on hyperparameters and training are required to encounter this phenomenon but are of this publication's scope.

The inverse function evaluation can now be performed in less than 20 ns and the results are sufficiently precise.

IV. EXPERIMENTAL VALIDATION

To demonstrate the general capability of reproducing experiments performed at the test bench introduced in [13], the soft pneumatic actuator is implemented in the C++ environment. It has to be kept in mind, that at this point, dynamics parameters are still tuned manually so this is but a preliminary showcase of the framework's capabilities.

The test bench contains a soft pneumatic actuator with three fibre-reinforced air chambers, each connected to source pressure or environmental pressure over a solenoid valve.

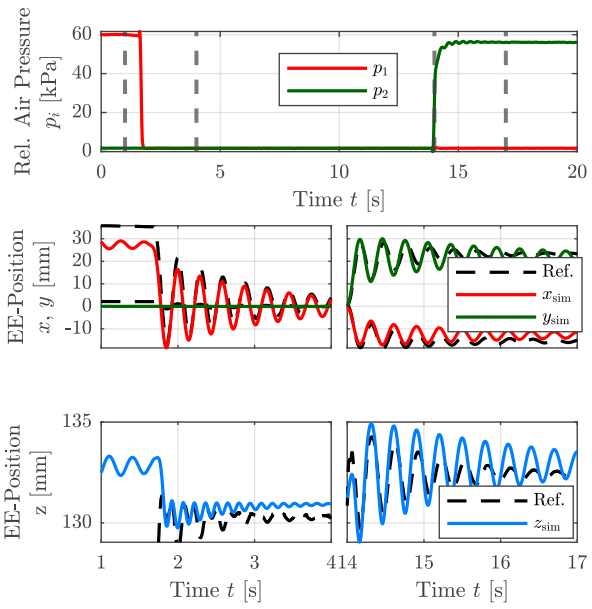

Fig. 7. Simulation results for data from experiments. In this experiment, a single chamber is directly connected to source pressure (60 kPa) or the environment by opening/closing the valves as fast as possible. Shown are the two responses of the end effector position for 1 s$<t<$4 s and 14 s$<t<$17 s.

Pressure is measured at the tube connectors directly behind the valve, leading to a slight delay between measured and actual pressure in the chambers. The SPA is made of three sections of which two are referred to as *caps*. These form the upper and lower end of a beam and are made of Dragonskin 30. The middle part is the actual *actuator*, contains the three air chambers, and is made of Ecoflex 0050. Position and orientation for validation are tracked via an OptiTrack Prime Camera-Marker system and base reaction forces and moments are measured with an ATI mini40 sensor between a 3D-printed rigid adapter and the socket.

The SMR model is implemented by stacking three rods serially and setting material and geometrical properties accordingly. Displacements in the *actuator* are computed with the identified neural network. For more details such as geometric parameters refer to [13]. Material parameters chosen for the *actuator* are listed in Table III. The mass of the marker plate at the tip is included in the model by appending an additional mass of 60 g to the SMR object. Damping coefficients were found heuristically by examining two experiments. At first, all chambers were synchronously connected to the source which leads to a quick rise in pressure in each chamber. Since no vibration was observed in experiments, the damping coefficient was increased until the model showed the same behaviour and the rise time matched with the experiments. In the second, bending motion is excited by a step in pressure of chamber one around 40 kPa, and parameters are adapted accordingly.

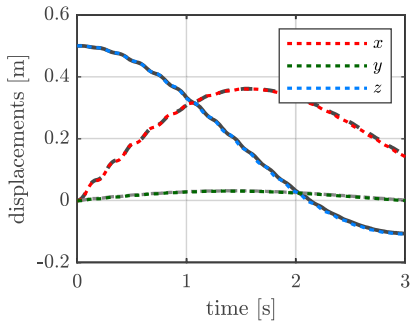

Fig. 8. Rebuilding the benchmark simulation in [23]. Coloured, dotted lines are the output from the simulation environment placed on top of the lines from the original figure from [23].

The pressure input is computed as a step in local forces

$$\boldsymbol{R}^{\mathrm{T}}\boldsymbol{n}(s^{+}) = \boldsymbol{R}^{\mathrm{T}}\boldsymbol{n}(s^{-}) + \sum_{i=1}^{3} p_i \alpha_{\mathrm{l}} A_{\mathrm{ch}}\, \boldsymbol{e}_z \qquad (24)$$

acting on the cross-section of the air chamber A_{ch} at intersections between the caps denoted by material coordinate s^{-} and the actuator denoted s^{+}. The lateral compression factor α_{l} is accounting for elongation effect caused by compression of material between fibre and air [15]. A corresponding jump in local moments is computed accordingly as

$$\boldsymbol{R}^{\mathrm{T}}\boldsymbol{m}(s^{+}) = \boldsymbol{R}^{\mathrm{T}}\boldsymbol{m}(s^{-}) + \sum_{i=1}^{3} p_i \alpha_{\mathrm{l}} A_{\mathrm{ch}}\, (\boldsymbol{d}_{\mathrm{ch},i} \times \boldsymbol{e}_z) \qquad (25)$$

with lever $\boldsymbol{d}_{\mathrm{ch},i}$ from centre of the actuator's cross-section to centre of the chamber's cross-section. Note that the last term in (24) and (25) has to be negative if s^{+} is the cap and s^{-} the actuator [13], [10].

The experiment, depicted in Fig. 7 shows dynamic response to steps from $60\,\mathrm{kPa}$ to $0\,\mathrm{kPa}$ for pressure p_1 and $0\,\mathrm{kPa}$ to $60\,\mathrm{kPa}$ for pressure p_2. This is a medium-sized excitation compared to a maximum pressure of $100\,\mathrm{kPa}$ at which the risk of damaging the actuator rises drastically. The simulation shows good accordance between tip position from measurements and position with an MSE $< 7\%$ for all DoFs regarding the total trajectory. After the second jump in pressure, the settling time of the oscillation differs for measured and simulated quantities. For a more detailed analysis and improvement, we intend to find more suitable parameters from dynamic FE simulation with the procedure introduced in Sec. III-B.

As for the static equilibrium points, the general relationship between FE model and experiments observed in [21] (being the stiffer bending and softer extensional behaviour) also shows for the rod simulation.

V. SIMULATION AND NUMERICAL EXAMPLES

In this section numerical examples and benchmarks are briefly demonstrated including

- a clamped rod experiment from [23] in Sec. V-A,
- a manipulator composed of three actuators in Sec. V-B.

TABLE III
GEOMETRIC AND NUMERICAL PROPERTIES OF SOFT MATERIAL MANIPULATOR (SMR)

Length of chambers / caps	$50\,\mathrm{mm}$ / $5\,\mathrm{mm}$
Total length of SMR	$180\,\mathrm{mm}$
Cross-sectional / chamber radius	$12\,\mathrm{mm}$ / $3\,\mathrm{mm}$
Centre chamber to centre actuator	$7\,\mathrm{mm}$
Total number of nodes	80
BDF-α coefficient α_{BDF} [10]	-0.3
Spatial integration method	second-order RUNGE-KUTTA
Time step Δt	$0.01\,\mathrm{s}$

A. Clamped-Rod Benchmark

An example of dynamics simulation from [23] is re-implemented using the shooting method. This includes a single, initially straight steel rod with a total length of $0.5\,\mathrm{m}$, a radius of $1\,\mathrm{mm}$, Young's modulus of $E = 210\,\mathrm{GPa}$ and Poisson's ratio of 0.3. A follower tip wrench as time-dependent load is configured and applied as boundary condition $\boldsymbol{n}^{*}, \boldsymbol{m}^{*}$. Numerical parameters have to be adapted in the back-end of the simulation and are set to $\alpha_{\mathrm{BDF}} = -0.3$ and $\Delta t = 10\,\mathrm{ms}$. A total number of 500 nodes is used. Input time series are configured using the SIMULINK environment.

This is used to verify the simulation in general, excluding any mistakes made in implementation. Fig. 8 shows the successfully performed test.

B. Multi-Segment Actuator

The object-oriented implementation allows for a quick connection of serial rods in C++ with varying material properties. As a demonstration, a soft-material robot (SMR) consisting of three serially connected actuators is set up. The material properties are configured according to the described visco-hyperelasticy in Table III, but for this numerical demonstration material density is reduced by 40% to achieve larger deflections. Numerical results depicted in the title image Fig. 1 do not represent any real system and is instead used for show-casing the presented tool.

VI. DISCUSSION, CONCLUSION & OUTLOOK

A modular, computationally efficient simulation of visco-hyperelastic Cosserat rods is integrated into the well-established SIMULINK environment. Material parameters of the nonlinear stiffness are identified utilizing an accurate FE simulation. A preliminary validation for dynamic experiments is presented. This extends the works done by Eugster et al. in [16] and combines them with those by Till et al. in [10]. The MSE between experimental data and the model for tip position over time lies around 7%. The proposed method enables the systematic design of soft robotic actuators in simulation with valid parametrization.

A. Computational Time and Implementation

The current implementation has not yet shown the computational performance of [10]. The reason for this is a lack of optimization in memory allocation in the ODE/PDE, which is

currently a target of re-factorisation. For dynamics, a single time step of the steel rod simulation on an Intel Core i5-8600K CPU @ 3.60 GHz has an average duration of 7.1 ms per 10 ms of simulated time, which is faster than real-time. The SMR depicted on Fig. 1 however required a total of 200 s for a total simulation time of 6 s, which is around 340 ms per 10 ms time step, leaving room for optimisation. No difference in the computational time of the linear or nonlinear material model is noticeable, which highlights the efficiency of the approach. The integration in SIMULINK allows for a rapid workflow and safes the work of creating and maintaining a graphical user interface.

B. Non-Linear Hyperelasticity

As for the often discussed necessity of nonlinearity in hyperelastic models, at least for material used in this paper, and even with external forces up to 50 N, the authors find it neglectable. The relevance of the degressive behaviour of Ecoflex 0050 within the range of 0–100% strain is questionable, which is lining up with the statements in [20], [5].

Still, other applications with different designs and materials require nonlinear material models according to [24]. Conceptually, the proposed methods for identification can easily be transferred to the dynamic material model by computing local strain velocities from dynamic FE simulation in the same numerical manner, which will be performed and validated in future works. Note, that a consistent derivation of damping parameters presented in [25] is, at least according to [26], only possible as long as small local strains are considered. A detailed discussion is out of this paper's scope.

C. Future Work

This study is an intermediate result for a coherent chain of methods for soft pneumatic actuator design including detailed FEM and fast dynamic simulations for controller design. Extensions regarding the identification procedure for damping parameters and building a simulation of the full plant including source pressure, valves and tubes are the current focus.

REFERENCES

[1] C. Armanini, F. Boyer, A. T. Mathew, C. Duriez, and F. Renda, "Soft robots modeling: A structured overview," *IEEE Transactions on Robotics (T-RO)*, pp. 1–21, 2023.

[2] M. A. Graule, C. B. Teeple, T. P. McCarthy, G. R. Kim, R. C. St. Louis, and R. J. Wood, "Somo: Fast and accurate simulations of continuum robots in complex environments," *IEEE International Conference on Intelligent Robots and Systems (IROS)*, pp. 3934–3941, 2021.

[3] F. Renda, F. Boyer, J. Dias, and L. Seneviratne, "Discrete Cosserat approach for multisection soft manipulator dynamics," *T-RO*, vol. 34, no. 6, pp. 1518–1533, 2018.

[4] F. Renda, C. Armanini, V. Lebastard, F. Candelier, and F. Boyer, "A geometric variable-strain approach for static modeling of soft manipulators with tendon and fluidic actuation," *IEEE Robotics and Automation Letters (RA-L)*, vol. 5, no. 3, pp. 4006–4013, 2020.

[5] F. Boyer, V. Lebastard, F. Candelier, and F. Renda, "Dynamics of continuum and soft robots: A strain parameterization based approach," *T-RO*, vol. 37, no. 3, pp. 847–863, 2021.

[6] A. T. Mathew, I. M. B. Hmida, C. Armanini, F. Boyer, and F. Renda, "SoRoSim: A Matlab toolbox for hybrid rigid-soft robots based on the geometric variable-strain approach," *IEEE Robotics & Automation Magazine*, pp. 2–18, 2022.

[7] J. Allard, S. Cotin, F. Faure, P.-J. Bensoussan, F. Poyer, C. Duriez, H. Delingette, and L. Grisoni, "Sofa – an open source framework for medical simulation," in *MMVR 15 - Medicine Meets Virtual Reality*, ser. Studies in Health Technology and Informatics, vol. 125. Palm Beach, United States: IOP Press, Feb. 2007, pp. 13–18.

[8] N. Naughton, J. Sun, A. Tekinalp, T. Parthasarathy, G. Chowdhary, and M. Gazzola, "Elastica: A compliant mechanics environment for soft robotic control," *RA-L*, vol. 6, no. 2, pp. 3389–3396, 2021.

[9] D. Trivedi, A. Lotfi, and C. D. Rahn, "Geometrically exact dynamic models for soft robotic manipulators," in *IROS*, 2007.

[10] J. Till, V. Aloi, and C. Rucker, "Real-time dynamics of soft and continuum robots based on Cosserat rod models," *International Journal of Robotics Research (IJRR)*, vol. 38, no. 6, pp. 723–746, 2019.

[11] S. M. H. Sadati, S. E. Naghibi, A. Shiva, I. D. Walker, K. Althoefer, and T. Nanayakkara, "Mechanics of continuum manipulators, a comparative study of five methods with experiments," in *Towards Autonomous Robotic Systems*. Springer International Publishing, 2017, pp. 686–702.

[12] H. B. Gilbert and I. S. Godage, "Validation of an extensible rod model for soft continuum manipulators," *2019 IEEE International Conference on Soft Robotics (RoboSoft)*, pp. 711–716, 2019.

[13] M. Bartholdt, M. Wiese, M. Schappler, S. Spindeldreier, and A. Raatz, "A parameter identification method for static Cosserat rod models: Application to soft material actuators with exteroceptive sensors," in *IROS*, 2021, pp. 624–631.

[14] M. Wiese, B.-H. Cao, and A. Raatz, "Towards accurate modeling of modular soft pneumatic robots: from volume FEM to Cosserat rod," in *IROS*, 2022, pp. 9371–9378.

[15] R. Berthold, M. Wiese, and A. Raatz, "Investigation of lateral compression effects in fiber reinforced soft pneumatic actuators," in *2022 International Conference on Electrical, Computer, Communications and Mechatronics Engineering (ICECCME)*, 2022, pp. 1–7.

[16] S. R. Eugster, J. Harsch, M. Bartholdt, M. Herrmann, M. Wiese, and G. Capobianco, "Soft pneumatic actuator model based on a pressure-dependent spatial nonlinear rod theory," *RA-L*, vol. 7, no. 2, pp. 2471–2478, 2022.

[17] H. B. Khaniki, M. H. Ghayesh, R. Chin, and M. Amabili, *A review on the nonlinear dynamics of hyperelastic structures*. Springer Netherlands, 2022, vol. 3.

[18] B. J. Caasenbrood, A. Y. Pogromsky, and H. Nijmeijer, "Dynamic modeling of hyper-elastic soft robots using spatial curves," *IFAC-PapersOnLine*, vol. 53, pp. 9238–9243, 2020.

[19] S. M. Mustaza, Y. Elsayed, C. Lekakou, C. Saaj, and J. Fras, "Dynamic modeling of fiber-reinforced soft manipulator: A visco-hyperelastic material-based continuum mechanics approach," *Soft Robotics*, vol. 6, no. 3, pp. 305–317, 2019.

[20] A. Shiva, S. M. Sadati, Y. Noh, J. Fraś, A. Ataka, H. Würdemann, H. Hauser, I. D. Walker, T. Nanayakkara, and K. Althoefer, "Elasticity versus hyperelasticity considerations in quasistatic modeling of a soft finger-like robotic appendage for real-time position and force estimation," *Soft Robotics*, vol. 6, no. 2, pp. 228–249, 2019.

[21] R. Berthold, M. N. Bartholdt, M. Wiese, S. Kahms, S. Spindeldreier, and A. Raatz, "A preliminary study of soft material robotic modelling: Finite element method and Cosserat rod model," in *2021 9th International Conference on Control, Mechatronics and Automation (ICCMA)*, 2021, pp. 7–13.

[22] M. Sonka, J. M. Fitzpatrick *et al.*, *Handbook of Medical Imaging, Volume 2. Medical Image Processing and Analysis*. Society of Photo-optical Instrumentation Engineers (SPIE), 2000.

[23] S. Grazioso, G. Di Gironimo, and B. Siciliano, "A geometrically exact model for soft continuum robots: The finite element deformation space formulation," *Soft Robotics*, vol. 6, no. 6, pp. 790–811, 2019.

[24] L. Marechal, P. Balland, L. Lindenroth, F. Petrou, C. Kontovounisios, and F. Bello, "Toward a common framework and database of materials for soft robotics," *Soft Robotics*, vol. 8, no. 3, pp. 284–297, 2021.

[25] J. Linn, H. Lang, and A. Tuganov, "Geometrically exact Cosserat rods with Kelvin-Voigt type viscous damping," *Mechanical Sciences*, vol. 4, no. 1, pp. 79–96, 2013.

[26] C. Meier, "Geometrically exact finite element formulations for slender beams and their contact interaction," Ph.D. dissertation, TU München, Germany, 2016.